Coupled Ocean–Atmosphere Covariances in Global Ensemble Simulations: Impact of an Eddy-Resolving Ocean

SERGEY FROLOV,[a,b,c] CAROLYN A. REYNOLDS,[c] MICHAEL ALEXANDER,[b] MARIA FLATAU,[c] NEIL P. BARTON,[c] PATRICK HOGAN,[b] AND CLARK ROWLEY[d]

[a] *Cooperative Institute for Research in Environmental Sciences, University of Colorado, Boulder, Colorado*
[b] *NOAA/Physical Sciences Laboratory, Boulder, Colorado*
[c] *Marine Meteorology Division, Naval Research Laboratory, Monterey, California*
[d] *Oceanography Division, Naval Research Laboratory, Stennis Space Center, Mississippi*

(Manuscript received 2 November 2020, in final form 25 January 2021)

ABSTRACT: Patterns of correlations between the ocean and the atmosphere are examined using a high-resolution (1/12° ocean and ice, 1/3° atmosphere) ensemble of data assimilative, coupled, global, ocean–atmosphere forecasts. This provides a unique perspective into atmosphere–ocean interactions constrained by assimilated observations, allowing for the contrast of patterns of coupled processes across regions and the examination of processes affected by ocean mesoscale eddies. Correlations during the first 24 h of the coupled forecast between the ocean surface temperature and atmospheric variables, and between the ocean mixed layer depth and surface winds are examined as a function of region and season. Three distinct coupling regimes emerge: 1) regions characterized by strong sea surface temperature fronts, where uncertainty in the ocean mesoscale influences ocean–atmosphere exchanges; 2) regions with intense atmospheric convection over the tropical oceans, where uncertainty in the modeled atmospheric convection impacts the upper ocean; and 3) regions where the depth of the seasonal mixed layer (MLD) determines the magnitude of the coupling, which is stronger when the MLD is shallow and weaker when the MLD is deep. A comparison with models at lower horizontal (1/12° vs 1° and 1/4°) and vertical (1- vs 10-m depth of the first layer) ocean resolution reveals that coupling in the boundary currents, the tropical Indian Ocean, and the warm pool regions requires high levels of horizontal and vertical resolution. Implications for coupled data assimilation and short-term forecasting are discussed.

KEYWORDS: Atmosphere-ocean interaction; Ensembles; Short-range prediction; Data assimilation

1. Introduction

Previous studies posited that coupling of the atmosphere with an eddy-resolving ocean model is essential for accurate weather and climate forecasts (Kirtman et al. 2012; Small et al. 2008; Masumoto et al. 2004; Ma et al. 2016; Hewitt et al. 2016). This imperative has spurred the development of operational coupled forecast models (Komori et al. 2018; Laloyaux et al. 2015; Saha et al. 2010); however, often at low (0.5°–1°) ocean resolution or with regional model configurations (Holt et al. 2011; Pullen et al. 2017). The application of coupled models to forecasting raises new questions about the propagation of uncertainty in the initial conditions across the ocean–atmosphere (OA) interface and the impact of the initial uncertainty on the fidelity of short-term forecasts (Pullen et al. 2017). Here, we address some of these questions by examining patterns of enhanced OA interactions in an ensemble of an assimilative, ocean-eddy-resolving, global coupled system—the Navy Earth System Prediction Capability (Navy-ESPC). The Navy-ESPC model (Barton et al. 2021) couples 1/12° ocean and ice models with a 1/3° atmospheric model.

Previous studies of OA interactions used a combination of observational datasets and free-running coupled models to document the impact that midlatitude SST fronts can exert on the atmospheric circulation, including the depth of the atmospheric boundary layer, surface wind speed and direction, precipitation, clouds, and, potentially, the storm track. We review this body of literature in section 2. Despite the depth of the existing literature on OA interactions, the use of coupled models for medium-range weather forecasting motivates a new set of research questions:

1) What are the hot spot locations for OA coupling? Specifically, where will a perturbation in one component readily translate to uncertainty in the other component?
2) How does the uncertainty in initial conditions propagate across the OA interface? What physical mechanisms determine the direction of uncertainty propagation in a coupled model?
3) What guidance do patterns of the OA coupling provide to the developers of data assimilation (DA) algorithms?
4) How does resolution affect the ability of a coupled model to capture realistic patterns of OA correlations?

Examination of the forecast error covariances (computed from an ensemble of coupled forecasts) provides an insight to the questions above. Modern data assimilation methods provide an estimate of the initial uncertainty in the form of an ensemble of (coupled) initial conditions. The coupled ensemble forecast from these initial conditions can illuminate the degree

Supplemental information related to this paper is available at the Journals Online website: https://doi.org/10.1175/MWR-D-20-0352.s1.

Corresponding author: Sergey Frolov, sergey.frolov@noaa.gov

DOI: 10.1175/MWR-D-20-0352.1

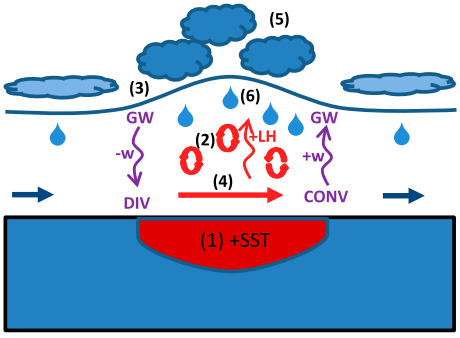

(1) Positive SST anomaly increases vertical mixing and the latent heat flux (2), which leads to deepening of the atm. boundary layer (3), entrainment of the momentum from the free atmosphere and increased surface winds (4), increased cloudiness (5), and precipitation (6). Precipitation is at maximum downwind of warm SST anomaly, where surface convergence is maximized.

As the cross gradient wind crosses from cold to warm water, surface wind divergence (DIV) arises that leads to downward anomaly in vertical velocities (-w) that is manifested in inertia gravity waves (GW) over the SST gradient. The opposite upward anomaly with GW occurs at the transition of cross gradient wind from warm to cold waters.

FIG. 1. Influence of a positive SST anomaly on the atmospheric boundary layer in a case of cross-gradient winds. Summary diagram and composition is influenced by the discussions and graphics from Wallace et al. (1989), Frenger et al. (2013), and Kilpatrick et al. (2016) among others.

to which the initial condition uncertainty is correlated across the OA interface. High cross-fluid correlations correspond to hot spots of local OA interactions. Examining different pairs of the coupled correlations (e.g., between SST and heat fluxes, precipitation, and clouds) together with the review of prior process-based studies can shed light on the mechanisms and the direction of the information flow across the OA interface. Finally, sensitivity of the OA correlations to the model configuration can shed light on the role that ocean resolution plays in the realism of the OA correlations and, hence, implications for the development of coupled DA methods.

Many previous studies have examined patterns of ocean and atmosphere correlations using monthly mean anomalies from annual climatology of free-running coupled models and observational data (Cayan 1992; Alexander et al. 2000; S. P. Bishop et al. 2017; Feng et al. 2018; Small et al. 2019). In contrast, here we compute OA correlations that emerge in the first 24 h of the coupled ensemble forecasts. While correlations of monthly anomalies provide information on perturbations to the seasonal cycle, the assimilative ensemble perturbations considered here represent the likely uncertainty in the analysis system. This focus on short-term correlations is both relevant for emerging applications of coupled DA and reflects recent findings in the process-based literature that the monthly average OA interactions can be dominated by a series of short-lived OA exchanges on the synoptic scale (Parfitt and Czaja 2016; O'Neill et al. 2017).

In this paper, we focus on examining two classes of OA correlations. First, we examine correlations between the SST and atmospheric variables, such as the 2-m temperature, precipitation, wind speed, cloud cover, and radiative and sensible heat fluxes. These correlations are dominated by the balance of heat exchange, radiation, and evaporation between the ocean surface and the atmosphere. Second, we examine correlations between the surface wind speed and the mixed layer depth, which are dominated by the momentum transfer between atmosphere and the ocean. We examine these correlations in three sets of runs: coupled runs with the eddy-resolving (1/12°), eddy-allowing (1/4°), and eddy-parameterized (1°) ocean models.

2. Background: Atmospheric response to ocean mesoscale SST fronts

There is an extensive body of literature on ocean atmosphere interactions and the response of the atmosphere to ocean mesoscale SST fronts. We review these prior studies here to motivate our inquiry and aid in interpretation of our results.

Enhanced OA coupling was documented by Chelton et al. (2001), who used newly available measurements from the QuikSCAT surface wind remote sensing satellite to document coupling between the low-level winds and the SST anomalies associated with tropical instability waves in the tropical east Pacific (TEPAC). Chelton et al. (2001) found that similar to the original hypothesis of Wallace (Wallace et al. 1989; Hayes et al. 1989) [and also summarized in Fig. 1], positive SST anomalies destabilize the atmospheric boundary layer and, as a result, enhance entrainment of momentum from the winds in the free atmosphere. Following the same logic, negative SST anomalies stabilize the atmospheric boundary layer and reduce entrainment of momentum from the free atmosphere, resulting in lower surface winds. This results in slower winds over the cold-water anomalies of the equatorial cold upwelling tongue. In the western boundary current regions, Chelton et al. (2004) showed that (similar to the TEPAC) the ocean SST fronts drive a significant portion of the variability in the local winds, heat, and moisture fluxes. Indeed, the vertical moisture flux in the Gulf Stream region can penetrate through the entire depth of the troposphere (Minobe et al. 2008; Small et al. 2008) and, once entrained in the storm track, can have significant impact on the path of the Atlantic storm track and on European precipitation (Kirtman et al. 2012; Vitart and Balmaseda 2018). Similar relationships have been documented for the Antarctic Circumpolar Current (ACC) (Byrne et al. 2016; Frenger et al. 2013). Chelton et al. (2004) also found that wind mixing is

important in frontal regions and depends on the orientation of the wind with respect to the front. For winds oriented along an SST front, wind curl dominates as stronger winds are mixed down to the surface on the warm side of the front resulting in quasigeostrophic Ekman pumping. Winds perpendicular to the front lead to divergence when the winds pass from the cold to the warm sector as the surface wind speed is enhanced over the warmer water, and likewise convergence occurs for wind directed from the warm to the cold side of the front.

In contrast to the atmospheric response to SST perturbations through (de)stabilization of the atmospheric boundary layer, other studies highlighted the importance of the pressure adjustment mechanism (e.g., Lindzen and Nigam 1987; Putrasahan et al. 2013) and the orientation of the atmospheric flow with respect to the SST gradient (Schneider and Qiu 2015; Kilpatrick et al. 2016). Lindzen and Nigam (1987) and Putrasahan et al. (2013) showed that enhanced local winds can result from a pressure gradient due to the density difference between the warm and moist air on the warm side of the SST front and the cold and dry air on the cold side of the SST front. For the case of cross-front winds (Fig. 1), surface wind stress divergence dominates and the vertical response exhibits an inertia–gravity wave similar to the mountain wave effect (Kilpatrick et al. 2016).

More recent studies (Small et al. 2019) showed that even in the midlatitudes, where SST gradients are common, the OA coupling behaves differently depending on the horizontal averaging scale chosen for the surface fluxes. For scales smaller than 500 km, the response of the atmosphere to SST gradients dominates (see description above and Figs. 1 and 2). To correctly simulate the direction of the OA fluxes on these small scales in midlatitudes requires coupled model forecasts with an eddy-permitting (about 25 km resolution) or eddy-resolving (less than 10 km resolution) ocean model. In contrast, for scales greater than 500 km, the atmosphere drives the SST anomalies via surface heat flux forcing and by influencing ocean mixing (Small et al. 2019; S. P. Bishop et al. 2017; Xie 2004).

In addition to the coupling between the winds and the SSTs, the warm ocean SST anomalies associated with mesoscale eddies and fronts can result in enhanced precipitation and cloud cover. The first instrumentally documented record of these effects dates back to the first weather-radar-based observations of the Gulf Stream current (Hobbs 1987). More recently these effects were documented using satellite observations in the Southern Ocean (Frenger et al. 2013). The local increase in the cloud cover and precipitation can be attributed to the response of the atmospheric boundary layer stability, atmospheric convection, and changes in the surface moisture supply to perturbations in the SST (Frenger et al. 2013; Minobe et al. 2008). Finally, recent papers suggest that the time-average OA interactions can be dominated by the intense but short-lived OA interactions on the synoptic scales (Parfitt and Czaja 2016; O'Neill et al. 2017).

In this paper, we use daily averaged fields to examine correlations on the short time scales. We contrast results in boundary current regions with other regions. We focus on analysis of correlations that are directly relevant to coupled DA and short-term forecasting. We seek to establish relationships between the correlations calculated in our system with the atmosphere–ocean interaction processes described in prior literature and also suggest physical mechanisms that might explain novel results.

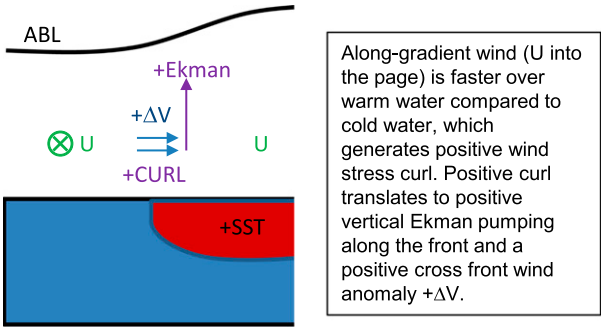

FIG. 2. Influence of a positive SST anomaly on the atmospheric boundary layer (ABL) in a case of alongfront winds (*U* directed into the page). Summary diagram and composition is influenced by the discussions and graphics from Kilpatrick et al. (2016).

3. Methods

a. Navy-ESPC model

1) COUPLED MODEL WITH EDDY-RESOLVING OCEAN

Navy-ESPC is the new coupled model developed by the U.S. Naval Research Laboratory to provide subseasonal forecasts of the coupled Earth system (Barton et al. 2021). Navy-ESPC comprises the Navy Global Environmental Model (NAVGEM) atmospheric model at 1/3° resolution (Hogan et al. 2014) and the Global Ocean Forecasting System (GOFS) at 1/12° resolution (Metzger et al. 2014). The GOFS system combines the Hybrid Coordinate Ocean Model (HYCOM; Bleck 2002), and the Los Alamos Sea Ice Model (CICE version 4; Hunke and Lipscomb 2015). HYCOM has 42 hybrid vertical levels with a top level of 1 m. The land model is implemented as a part of the atmospheric model (Hogan 2007). The coupled model uses the Earth System Modeling Framework (ESMF; (Hill et al. 2004; Theurich et al. 2016) to exchange fields within the bulk formula parameterizations hourly, including 10-m wind, 2-m temperature and humidity, downwelling shortwave and longwave fluxes at the surface, and precipitation rates. NAVGEM and HYCOM compute fluxes independently using the COARE V3.0 algorithm (Fairall et al. 2003; Kara et al. 2005) based on a common set of exchanged fields. To improve representation of the Madden–Julian oscillation, NAVGEM uses a modified Kain–Fritsch convection scheme (Kain and Fritsch 1990; Ridout et al. 2005) instead of the simplified Arakawa–Shubert scheme used in the uncoupled version of NAVGEM (Hogan et al. 2014).

Initial conditions for the 24-h forecast are estimated using a weakly coupled DA approach. Following the convention of Penny et al. (2017), in the weakly coupled system the coupled model provides the first guess for DA but no error cross correlations between components (e.g., between the atmosphere and the ocean) are used in the generation of the initial

conditions. We use the Hybrid-4DVAR system of Kuhl et al. (2013) for atmospheric initial conditions and the 3DVAR-FGAT system of Cummings and Smedstad (2014) for ocean and ice initial conditions. Cummings and Smedstad (2014) and Frolov et al. (2020) provide a comprehensive list of observations included in the ocean and atmospheric data assimilation systems.

The ocean, ice, and atmospheric DA systems use assimilation windows of different lengths. The atmospheric Hybrid-4DVAR updates the atmospheric state every 6 h, with DA windows centered on 0000, 0600, 1200, and 1800 UTC. Ice and ocean DA update initial conditions daily during a 24-h DA window centered at 1200 UTC. In other words, for each ocean and ice update, there are four atmospheric updates. A 3-h-long incremental analysis update is used to minimize the initialization shocks and to synchronize the components of the system before the next data assimilation window starts.

2) Ensemble forecast system

The Navy-ESPC system employs the ensemble of data assimilations (EDA) approach (Houtekamer et al. 1996; Isaksen et al. 2010) to generate an ensemble of initial conditions for the forward model. Our EDA system uses 16 ensemble members. Member 1 is the traditional deterministic data assimilation and forecast system. Members 2–16 are replicates of member 1 but with observational data perturbed with random noise consistent with the observation error covariances assumed by the DA systems. Observations are perturbed for all components of the system: atmosphere, ocean, and ice. The resulting system is known to exhibit deficient ensemble spread as compared to observed forecast errors (Bowler et al. 2017; Barton et al. 2021). We plan to address this deficiency in later versions of the system.

Our EDA system was cycled from 15 December 2016 to 1 February 2018 (see Barton et al. (2021) for the description of the cycling system). Once a week (starting from 1 February 2017), a 60-day forecast was issued at 1200 UTC after the initial 3-h IAU period was applied. All of the work presented in this paper analyzes the first 24 h of the weekly 60-day forecasts.

3) Mixed layer depth computation

Mixed layer depth (MLD) used in this paper is the diagnostic output of the HYCOM model that is computed on the native tripolar horizontal grid and the hybrid vertical coordinates using the native density variable of HYCOM. The density criteria used to establish the MLD is equivalent to a 0.3 K jump across the MLD interface. The MLD is computed for each ensemble member. The ensemble mean MLD is obtained by averaging MLD for individual members and not by calculating the MLD for ensemble averaged salinity and temperature to avoid using the smoothed vertical gradients in the 3D salinity and temperature fields of the ensemble mean forecast.

b. Low-resolution version of the NAVY-ESPC model

To examine the impact of ocean resolution on the OA correlation patterns, we reran the ensemble forecasts described in section 3.1.2 in the ocean-eddy-allowing configuration (1/3° atmosphere, 1/4° ocean, and 1/4° ice). We retained the same vertical resolution in both the ocean and the atmosphere. The initial conditions for this reforecast dataset were generated from the eddy-resolving initial conditions generated by the cycling EDA system from section 3.1.2 that used 1/12° resolution for the ocean component of the coupled model, by smoothing and interpolating them to the coarser grid.

c. CERA-20C dataset

To examine correlation relationships in the coupled ensemble with parameterized ocean eddies, we used the CERA-20C dataset from ECMWF (Laloyaux et al. 2015). CERA-20C used 1° horizontal resolution for all components of the Earth model and 10-m vertical resolution for the first layer of the ocean model. The daily ensembles of forecasts were downloaded from the ECMWF MARS archive for every other month of 2007 (starting from February 2007). The daily averages were computed by averaging 0600 and 1800 UTC publicly available forecasts. We downloaded data for 2007 because CERA data were not available for 2017, when the Navy-ESPC archive was produced. Because of these multiple differences in the sampling between the Navy-ESPC and CERA, we will confine our discussion to qualitative comparisons of patterns and we will not assign any statistical significance to these differences.

d. Index of SST–wind speed correlation

To quantify the propensity of each grid cell (indexed by the counter i) to have positive or negative correlations over the year, we used the following index:

$$F(i) = \frac{N_{\mathrm{corr}(i)>\mathrm{thr}} - N_{\mathrm{corr}(i)\le -\mathrm{thr}}}{N_{\mathrm{corr}(i)>\mathrm{thr}} + N_{\mathrm{corr}(i)\le -\mathrm{thr}}}, \tag{1}$$

where N is the number of times when the correlation with a quantity of interest was either greater ($N_{\mathrm{corr}(i)>\mathrm{thr}}$) or smaller ($N_{\mathrm{corr}(i)<\mathrm{thr}}$) than a given threshold. We used the threshold of 0.1 to omit cases when the magnitude of the correlation was too small to be meaningfully[1] considered positive or negative. To reduce noise in correlations due to the small ensemble size, we spatially average the correlations in Eq. (A3). The spatial averages were computed using a centered 5° × 5° box-car filter.

Values $F(i)$ are bound between $[-1, 1]$. Positive values of $F(i)$ indicate that positive correlations are more common than negative correlations over the 12-month record, and vice versa.

4. Results

a. Correlations between SST and atmosphere

Over the annual cycle, the global ocean can be divided into three categories based on the prevalent sign of the SST–wind speed correlations [index $F(i)$ in Eq. (1)]: 1) regions dominated by positive SST–wind speed correlations (red shading), 2) regions dominated by negative SST–wind speed correlations

[1] Using 16 ensemble members, averaging over a 5 × 5 box of grid points, and ignoring reduction in the degrees of freedom due to autocorrelation, correlation coefficients greater than 0.08 are statically significant at $p = 0.1$.

(blue shading), and 3) regions where neither negative nor positive correlations dominate (white shading) as shown in Fig. 3a. We chose the correlations between the SST and the wind speed as the basis for our classification because positive correlations typically indicate SST perturbations driving the atmospheric response and negative correlations indicate that the ocean is responding to atmospheric perturbations (Saravanan and Chang 2019).

Areas where correlations are predominantly positive through the year (red shading within a black contour line) overlap with regions of strong SST gradients (Fig. 4a) and large SST ensemble variance (Fig. 4b). This finding is in accord with the extensive literature on the response of the atmosphere to SST fronts reviewed in section 2 and is described further in section 4a(1). In section 4a(1), we also examine the annual cycle of three regions with positive correlations: the Gulf Stream (region 1), the Falklands Current (region 2), and the tropical east Pacific (region 3) outlined with red lines in Fig. 3a.

Review of the areas with predominantly negative correlations through the year (blue shading within a black contour line) indicate that these areas overlap with areas of enhanced atmospheric convection (as indicated by persistent cloud cover and large precipitation amounts in Figs. 4c and 4d) and areas with very shallow oceanic mixed layers (Figs. 4e and 4f). Most of these areas are contained within the warm pool (region 4) and the tropical Indian Ocean (region 5). The Pacific subtropical convergence zones exhibit slightly more negative correlation values (region 6). We examine the annual cycle of these three regions with negative correlation and diagnose the direction of the fluxes in section 4a(2).

Regions that do not demonstrate annual-averaged preference for either negative or positive SST–wind speed correlations (white shading in Fig. 3a) can be further subdivided into regions with an annual cycle with marked positive and negative correlations that cancel in the annual average and regions where correlations are very small through most of the year. To separate between these two cases, Fig. 3b shows the frequency with which correlations exceeded our target criteria of 0.1. Regions in deep blue (outlined with the 30% isoline) do not show strong correlations between wind speed and SST through most of the year (at least 70%) and will not be examined further. However, many of the regions do have correlations exceeding the threshold through most of the year. We will examine one such region (southern Pacific) in more detail in section 4a(3).

To summarize, our analysis suggests that the global pattern of the OA correlations can be roughly segmented into three regions:

1) Regions dominated by strong SST fronts, where ocean perturbations drive the atmospheric response;
2) Tropical ocean, where perturbations in atmospheric convection drive the ocean response; and
3) Regions where the seasonal changes, including the depth of the ocean mixed layer, determine the sign of the OA correlations.

We note that the proposed categorization is far from exhaustive and further distinctions between regions might be relevant for specific applications.

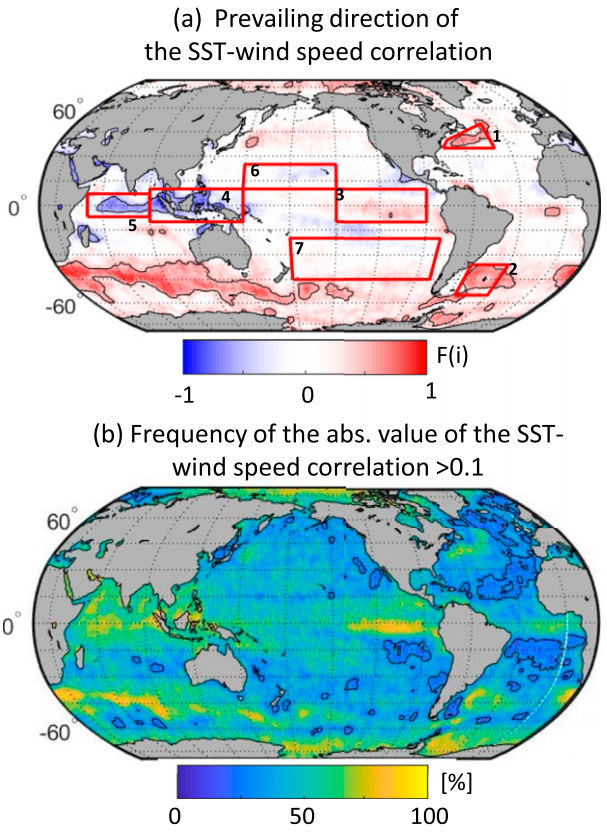

FIG. 3. (a) Prevalence of positive (red colors) or negative (blue colors) direction of SST–wind speed correlations in the annual cycle, computed using $F(i)$ from Eq. (3). Black contour indicates −0.5 and 0.5 isolines. Study regions are outlined with red boxes and include 1) Gulf Stream, 2) Falklands, 3) tropical east Pacific, 4) warm pool, 5) tropical Indian Ocean, 6) North Pacific subtropical convergence zone, 7) South Pacific midlatitudes. (b) Frequency of the absolute value of the SST–wind speed correlations exceeding the threshold of 0.1. Black isoline drawn for frequency of 30%.

1) REGIONS DRIVEN BY THE MESOSCALE VARIABILITY OF SST GRADIENTS

Ocean regions with strong SST gradients include western boundary currents (such as Gulf Stream, the Kuroshio, and the Somali Currents), elements of the Antarctic Circumpolar Current (such as Agulhas and Falklands retroflection regions), the eastern boundary currents (such as Humboldt, Benguela, and California Currents), currents associated with equatorial upwelling in the tropical east Pacific (TEPAC), and equatorial counter currents (e.g., the Southern Indian Counter Current). The locations of such areas can be seen in Figs. 4a and 4b that show magnitudes of SST gradients and the standard deviation of the SST ensemble. In fact, there is a strong correspondence between the strength of the SST gradients in the control member of the ensemble (Fig. 4a) and the standard deviation of the ensemble SST (Fig. 4b). We attribute this correspondence to the fact that in the eddy-resolving ensemble most of the SST ensemble spread is due to the uncertainty in the location of ocean features with strong SST gradients (such as

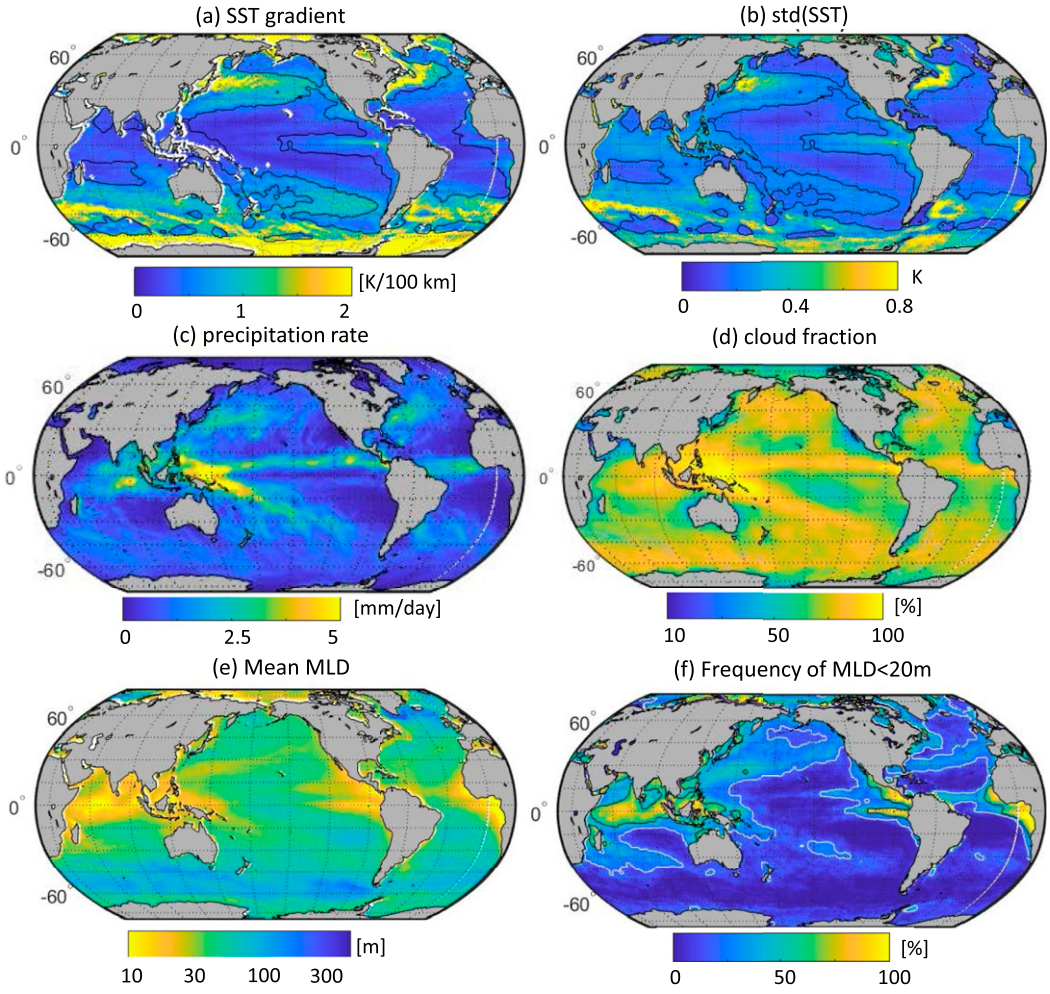

FIG. 4. Annual averages of (a) SST gradient, isoline is drawn for std(SST) = 0.2 K. (b) Ensemble standard deviation for SST, isoline is drawn for std(SST) = 0.2 K. (c) Model precipitation climatology. (d) Model cloud fraction climatology. (e) Mean mixed layer depth (MLD). (f) Frequency of MLD shallower than 20 m; the isolines indicate frequency of 80% (black) and 20% (gray).

western boundary currents). To facilitate visual comparisons between multiple maps in the paper, we will use the contour line of SST STD equal to 0.2 K as a common reference in Figs. 5 and 11. This contour line is only used as a visual guide and we do not assign any specific dynamical interpretation to this value.

Figure 5 shows that regions of strong SST gradients [above 1.5K $(100\,\text{km})^{-1}$ or SST STD of 0.6 K] exhibit positive correlations of SST[2] perturbations with air temperature (Fig. 5a), total precipitation (Fig. 5b), wind speed (Fig. 5c), total cloud cover (Fig. 5d), and sensible and latent heat fluxes (Figs. 5e and 5f). The same regions show slightly negative correlation with net radiative fluxes (Figs. 5g,h). These correlation patterns are consistent with prior observational findings (Small et al. 2008; Chelton et al. 2001; Chelton and Xie 2010; Deser et al. 1993; Frenger et al. 2013; Hobbs 1987; Wu and Kirtman 2007) that are characteristic of regions where the ocean drives the variability in the atmosphere (Saravanan and Chang 2019). A summary of these prior findings is described schematically in Figs. 1 and 2. In the presence of a strong SST gradient, a change in SST is often associated with ocean mesoscale activity that introduces SST perturbation in the form of an SST front associated with tropical instability waves, Gulf Stream meanders, or "squirts and jets" of the upwelling currents. A positive perturbation in the SST leads to an increase in surface winds (positive correlations in Fig. 5c) and enhanced turbulent heat fluxes (positive correlations in Figs. 5e and 5f), which is consistent with prior findings (Minobe et al. 2008; Small et al. 2008). The same increase in SST leads to an increase in the overlaying atmospheric temperatures (supported by positive correlations

[2] Note that over the ice-covered areas, the SST switches to the ice surface temperature. For that reason, we ignore analysis of correlations in this paper in the high-latitude regions with seasonal ice cover.

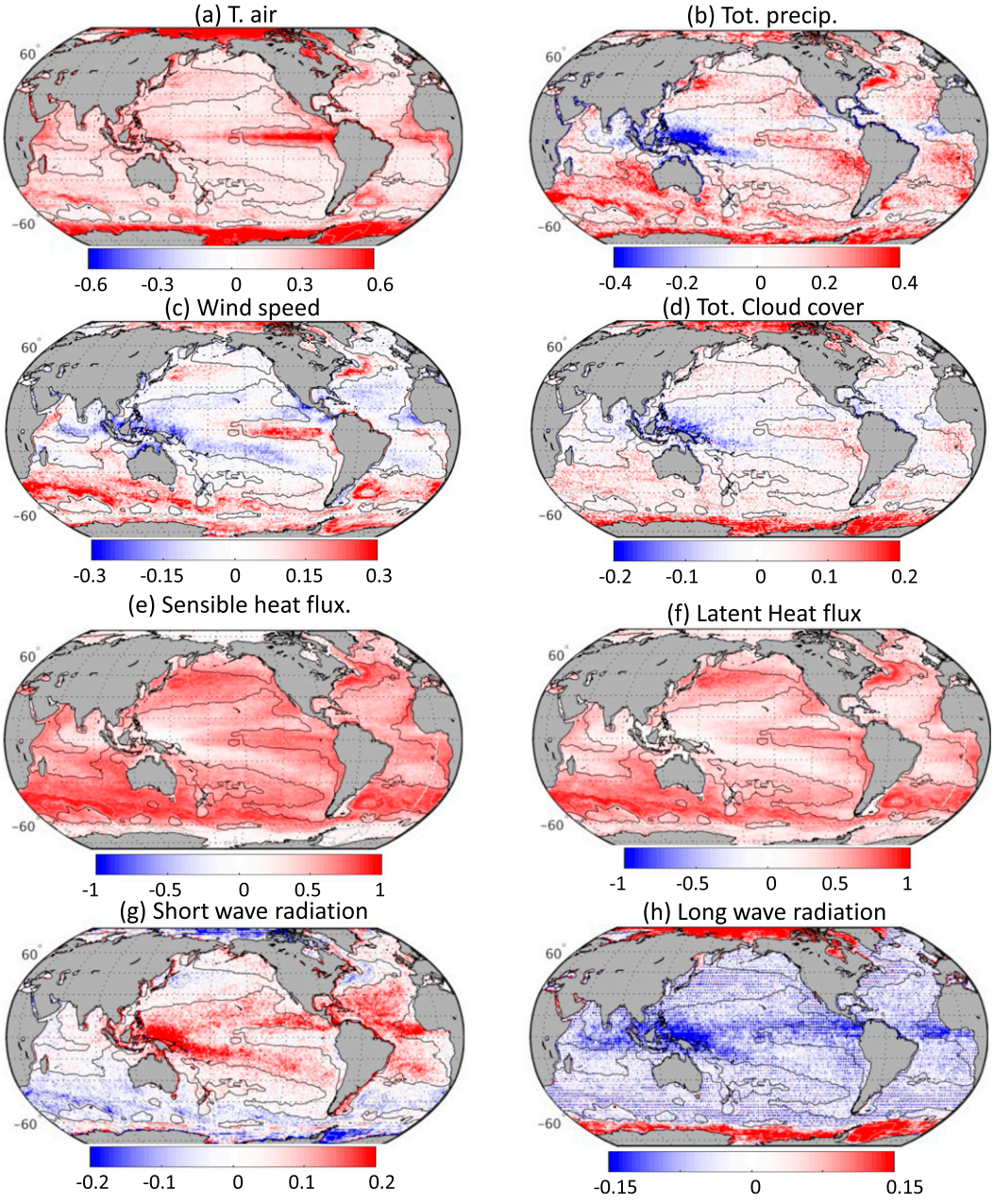

FIG. 5. Annual average of correlations between SST and (a) air temperature at 2 m, (b) total precipitation, (c) wind speed, (d) total cloud cover, (e) sensible heat flux, (f) latent heat flux, (g) shortwave heat flux, and (h) longwave heat flux in the Navy-ESPC ensemble. For radiative fluxes in (g) and (h), the positive direction is downward (positive correlation indicates warmer ocean temperatures correlate with increased radiative forcing of the ocean) and for turbulent fluxes in (e) and (f) the positive direction is upward (positive correlation indicates that warmer SST correlates with increased flux into the atmosphere). Contour lines indicated average STD of the SST of 0.2 K (gray). Note that different panels use different color scales.

in Fig. 5a) and enhanced turbulence in the atmospheric boundary layer, which is consistent with prior findings (Chelton et al. 2001; Frenger et al. 2013). Enhanced latent heat flux (Fig. 5f) and elevated mixing in the boundary layer lead to increased cloudiness (Fig. 5d) (Deser et al. 1993) and precipitation (Fig. 5b) (Hobbs 1987). In turn, the increased cloud cover (Deser et al. 1993), reduces the incoming solar radiation (negative correlation in Fig. 5g).

The magnitude of the SST correlation with total precipitation and the wind speed is highest for the western boundary currents in the local hemisphere winter months when the gradient between the warm waters of the ocean and the cold

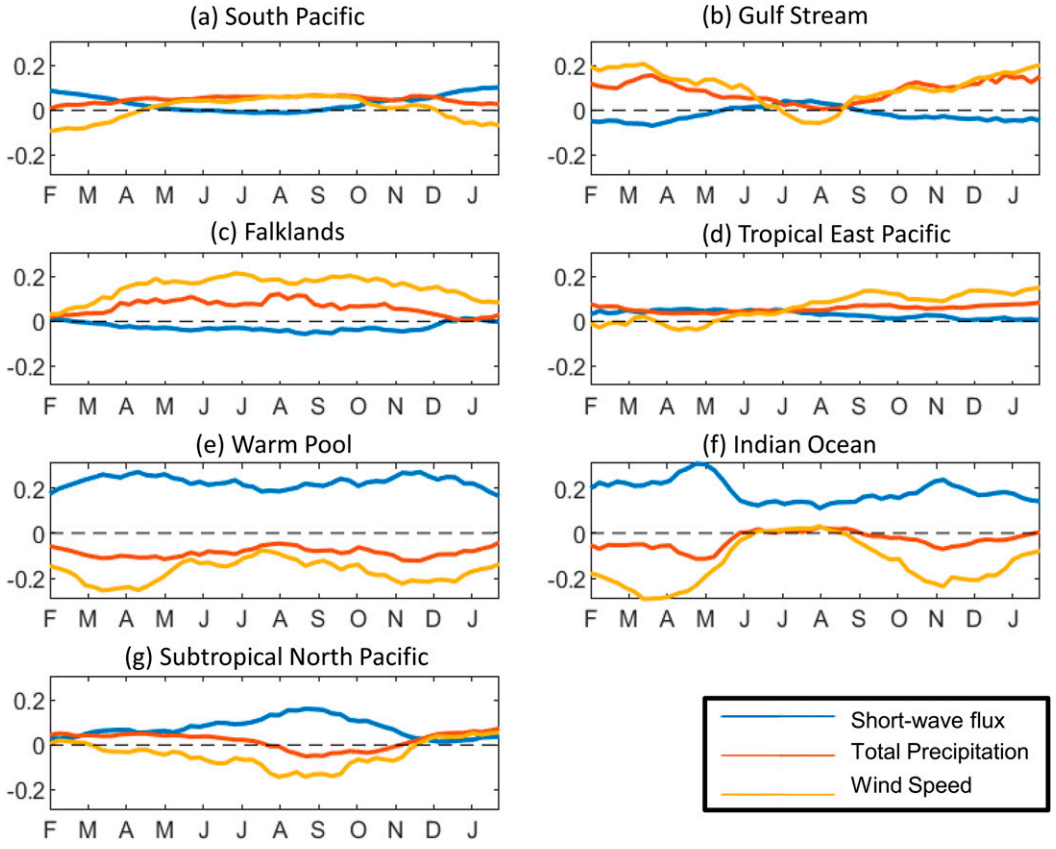

FIG. 6. Annual cycle of regionally averaged correlation between SST and total precipitation (blue), total flux (red), and wind speed (yellow). Spatial averages are computed over (a) South Pacific Ocean, (b) Gulf Stream, (c) Brazil–Falkland confluence region, (d) tropical east Pacific, (e) warm pool, (f) tropical Indian Ocean, and (g) the subtropical North Pacific. Locations of the averaging regions are shown in Fig. 3. Note that regional averages were computed for number of points between 300 (Gulf Stream) and 2600 (South Pacific). For such large number of grid points, the average correlation coefficient is significant at very low magnitudes ~0.01.

outflow from the continents is the highest (see the annual time series of the correlations in Figs. 6b–d). In summer, the sign of the correlation for SST–wind speed and SST–heat flux can reverse (e.g., in the month of August in the Gulf Stream region Fig. 6c), indicating the reversal of the influence in local summer, when the atmosphere starts to influence the surface ocean variability. As discussed in further detail in section 4a(3) below, we attribute this to the shallowing of the seasonal mixed layer to about 20 m (Fig. 7).

2) OA INTERACTIONS IN THE AREAS DOMINATED BY ATMOSPHERIC CONVECTION

In the regions of strong atmospheric convection, the sign of the correlation is often the opposite of regions dominated by strong SST gradients. We examine three of these regions in detail: tropical warm pool (region 4 in Fig. 3a), tropical Indian Ocean (region 5), and the subtropical North Pacific (region 6). The tropical warm pool and the tropical Indian Ocean are often characterized by SSTs in excess of 28°C that promote and sustain strong atmospheric convection with associated rainfall (Figs. 4c,d). The subtropical regions are characterized by a period of convection associated with the monsoon. Following Meehl (1987), we use a broad definition of the monsoon as a seasonal shift in precipitation and wind patterns in the tropics and subtropics due to differential heating of the continents and ocean and seasonal shifts in the intertropical convergence zones.

On subseasonal time scales, atmospheric convection is modulated by the active and inactive phases of the Madden–Julian oscillation (MJO)—a large-scale wave pattern of enhanced convection that circles the globe in 30–60 days—as well as by convectively coupled equatorial waves. However, in the context of this paper, we are interested in how the coupled system responds over a 24-h forecast to perturbations of the convective strength in the ensemble members (relative to the mean analysis of the convective state). For example, during an active MJO or monsoon phase all ensemble members might be experiencing active convection. However, the daily averaged intensity of this convection can be different between the ensemble members, which can affect the state of the ocean surface.

The mechanics of the OA interaction in the convectively active areas are summarized in Fig. 8. The cases of reduced convection are characterized by fewer clouds (Fig. 5d), less precipitation (Fig. 5b), and lighter winds (Fig. 5c). This meteorological

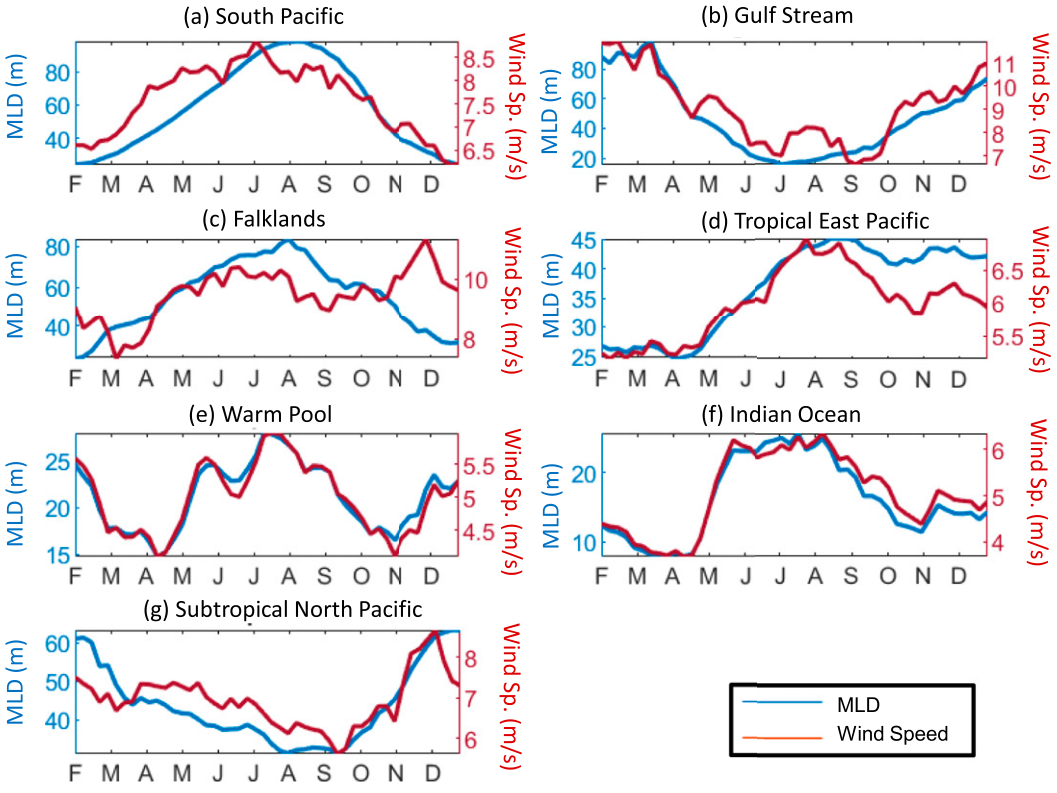

FIG. 7. Annual cycle of regionally averaged MLD (blue) and wind speed (red) in the Navy-ESPC ensemble. Spatial averages are computed over (a) South Pacific Ocean, (b) Gulf Stream, (c) Brazil–Falkland confluence region, (d) tropical east Pacific, (e) warm pool, (f) tropical Indian Ocean, and (g) the subtropical North Pacific. Locations of the averaging regions are shown in Fig. 3.

pattern leads to an increase in shortwave radiation (Fig. 5g) that warms the SST, which increases surface ocean stratification and suppresses vertical mixing. This suppression can be further amplified in the presence of diurnal warm layers (Matthews et al. 2014). Combined with lighter winds, this increased stratification leads to a shallower oceanic mixed layer. These correlation patterns are indicative of the atmosphere driving the ocean.

Seasonally, the OA correlations are enhanced during the periods with lighter winds and, hence, with a shallower MLD. For example, in the case of the tropical Indian Ocean and the warm pool, the wind are lightest (below 5 m s^{-1}) and the MLD is shallowest (shallower than 20 m) during spring and fall seasons (Figs. 7e,f). During this period, the correlations are also stronger (Figs. 6e,f). We attribute the enhanced MLD and OA correlation strength to the fact that an atmospheric perturbation of equal magnitude will have a larger impact on the surface ocean if the MLD is shallower. The pattern of shallower MLD in Fig. 7 is consistent with the annual cycle of the monsoon described in Meehl (1987).

3) OA INTERACTIONS MODULATED BY OCEANIC MIXED LAYER DEPTH

Feng et al. (2018) and Laloyaux et al. (2018) documented that in the CERA system, OA correlations in the midlatitudes follow the seasonal cycle of the MLD. During local summer, when MLD is shallow, the correlations between SST and 2-m temperature are enhanced; and during the local winter they are close to zero. We observe similar behavior of OA correlations

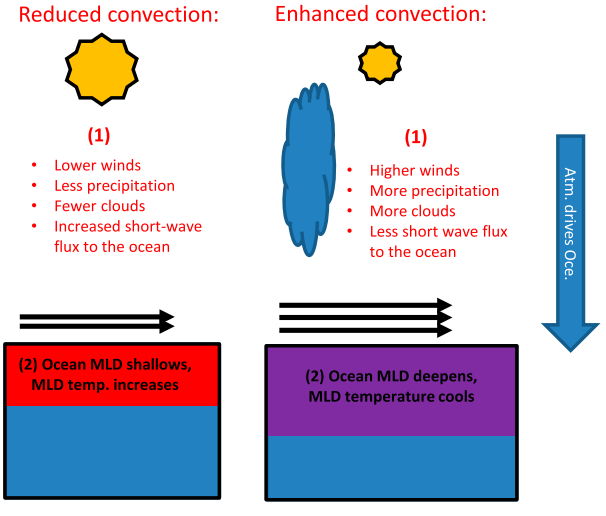

FIG. 8. Response of the tropical ocean to perturbations in the atmospheric convection.

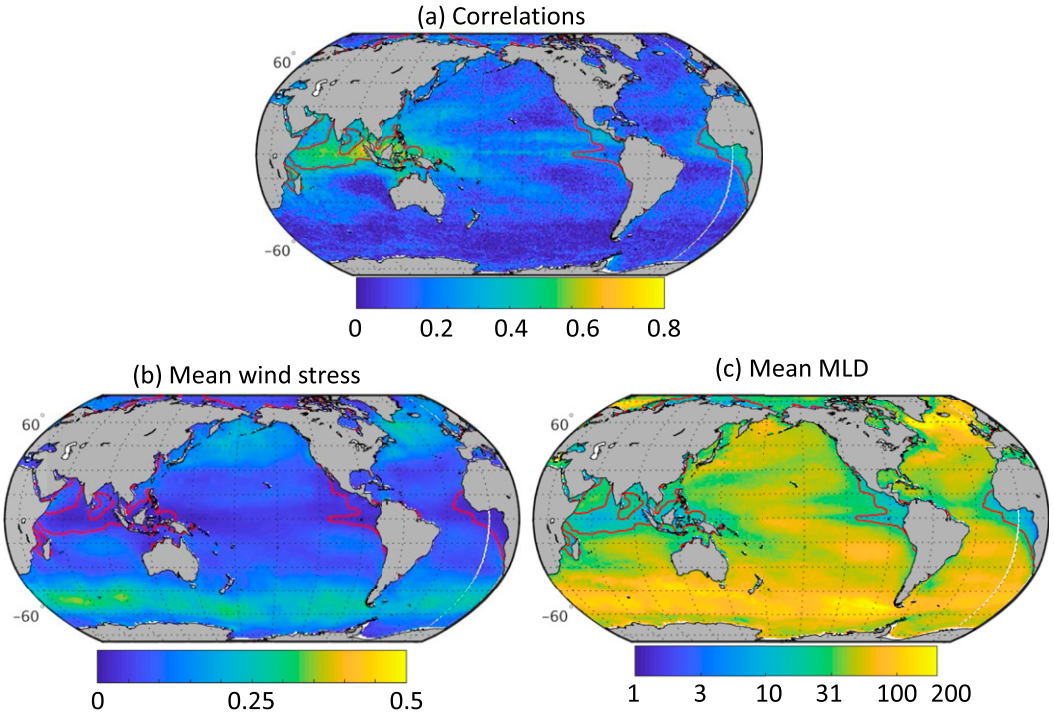

FIG. 9. Annual average correlations between wind stress magnitude and mixed layer depth in the Navy-ESPC ensemble: (a) correlation, (b) mean wind stress magnitude, and (c) mean MLD. Red contour delineates the average MLD of 20 m.

in the midlatitudes for correlations between SST and 2-m temperature (e.g., Fig. S1a in the online supplemental material for the South Pacific). We find that the magnitude of correlation is enhanced during the local summer when the average wind speed drops from a wintertime average of 9 m s^{-1} to about 7 m s^{-1}, which leads to a shallowing of the MLD from a wintertime maximum of 90 m to a summertime minimum of 20 m (Fig. 7a). Similar patterns were observed for the North Pacific (not shown).

However, unlike the previous studies in the CERA system (Feng et al. 2018; Laloyaux et al. 2018), we also find that MLD modulates the strength of the OA correlations in the tropical and subtropical regions [see section 4a(2)], where the strength of the winds and consequently the depth of the mixed layer are modulated by the seasonal monsoon. For example, in the Indian Ocean the winds are stronger during the summer monsoon season leading to a deeper oceanic mixed layer (Fig. 7f).

Also, in addition to the previous findings of Feng et al. (2018), we find that the sign of the wind speed–SST correlations in the midlatitudes can reverse from negative in local summer to positive in local winter (e.g., Figure 6a for the South Pacific). The OA interactions in the local summer (and in the presence of a shallow MLD) are consistent with the traditional view of the atmosphere driving the ocean (Xie 2004; Small et al. 2008). During the shallow MLD periods, positive SST perturbations are negatively correlated with the wind speed, which indicates that increased wind speed cools a shallow mixed layer through enhanced vertical mixing and enhanced upward turbulent fluxes. During the local winter in the midlatitudes (and in the presence of a deeper mixed layer) the correlation between SST and wind speed reverses sign (Fig. 6a for the South Pacific). The sign of the correlations (positive for precipitation and wind speed) are indicative of the ocean driving the atmosphere. Note that in the presence of strong boundary currents (Falklands and the Gulf Stream regions in Figs. 6b,c) the OA exchanges are dominated by strong SST gradients and are instead attenuated rather than reversed between the summer and winter. This reversal of the OA correlations in presence of the deep MLD has not been documented in the literature to our knowledge and is further discussed in the conclusions section.

b. *Correlations between MLD and wind stress*

Our analysis shows that perturbations in the daily wind speed affect MLD more strongly when the ambient MLD is already shallow. For example, Fig. 9 shows that for the annual average, areas with strong MLD–wind stress correlations overlap with regions were the MLD is shallower than 20 m (highlighted with a red contour line). Such dependence on MLD reflects the fact that it takes more work to mix a deep-water column than a shallow one. Hence, the same magnitude of the wind perturbation will affect regions of shallower MLD with more ease. This is consistent with the finding of Alexander and Penland (1996) that wind work dominates ocean mixing in summer months and deep convection dominates ocean mixing in winter (see Fig. S2 for the annual cycle of correlations). Additionally, the strength of the coupling between wind stress and the MLD is stronger in the west Pacific and the Indian Oceans (where the mixed layer is often separated from the

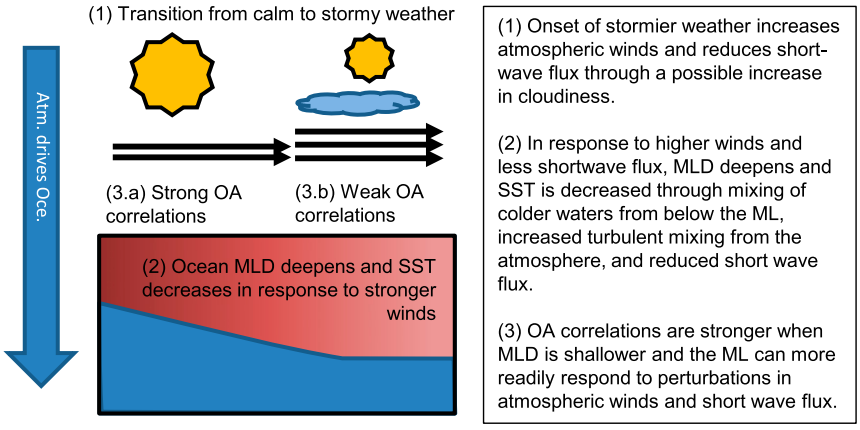

FIG. 10. Response of the ocean with shallow MLD to increased atmospheric storminess.

thermocline) than in the east Pacific (where the mixed layer and the thermocline variability is often consistent and strongly influenced by nonlocal ocean dynamics).

The relationship between the ambient MLD and the strength of the wind stress–MLD correlation is also apparent in the maps of the seasonally averaged correlations (Fig. S2). In Fig. S2, strong correlations in the midlatitudes correspond to seasonal shallowing of the MLD. Further investigation of the relationship between MLD and wind stress shows that this relationship holds even for episodic events. Figure S3 shows three consecutive weeks of the correlations, with stronger correlations corresponding to periods of weak winds and associated shallow MLD. This is especially prominent in the tropics, where high solar radiation reestablishes a shallow MLD in the presence of weak winds. In this case, periods of high correlations are greatly diminished by episodes of stronger winds that deepen the mixed layer beyond 20 m. A summary of this mechanism is presented in Fig. 10.

5. Impact of resolution on the correlations

Section 4 documents patterns of OA correlations in a coupled model with an eddy-resolving ocean component: horizontal resolution of 1/12° and 1 m thickness for the top layer of the ocean model. Do these correlation patterns hold in models with coarser ocean resolution? As a point of comparison, we will use the Navy-ESPC forecasts with reduced horizontal ocean resolution (1/4°) and the ECMWF's CERA ensemble system (1° horizontal resolution in the atmosphere and ocean, and 10 m top vertical resolution in the ocean). CERA uses a similar design for generation of the ensemble perturbation based on the ensemble of data assimilation methodology. However, CERA uses a different coupled model and data assimilation than the Navy-ESPC system, and the time period considered is different as CERA was not available for 2017.

Figure 11 shows maps of the annual-average correlations between the SST and the atmospheric fields in the eddy-resolving ensemble (left column), eddy-permitting ensemble (middle column) and eddy-parameterized ensemble (right column). Overall, the reduction in the ocean resolution reduces the impact of the ocean on the atmosphere, which is evident through:

1) An increase of negative correlation magnitudes between SST and wind speed (indicating that the atmosphere drives the ocean through enhanced mixing and surface heat fluxes)
2) A reduced magnitude of correlation between SST and precipitation (indicating that SST perturbations in low-resolution ocean models no longer translate to enhanced latent heat flux and associated local increases in precipitation)
3) An increased positive correlation between shortwave flux and the SST (indicating that perturbations in atmospheric cloudiness can directly translate to changes in the SSTs).

Detailed comparisons with the eddy-permitting version of the Navy-ESPC model (cf. left and central columns in Fig. 11) show marked differences in the OA correlations compared to the eddy-resolving version of the model. While the eddy-permitting version allows for the presence of SST gradients in the vicinity of the boundary currents, the magnitude of these correlations and the magnitude of the SST variance is greatly reduced (see gray isoline for SST STD in Fig. 11). Over the rest of the ocean, the OA interactions in the eddy-permitting model are dominated by the atmosphere driving the SST perturbations through fluctuations in the atmospheric shortwave flux. This is especially prevalent in the tropical Indian Ocean, where the eddy-resolving simulation has almost no correlation between SST and shortwave radiation, while the eddy-permitting simulation has a strong correlation. We attribute this to the lower internal variability of the ocean in the low-resolution simulation that allows the ocean to respond linearly to perturbations in the shortwave radiation. In contrast, we hypothesize that in the high-resolution ocean simulation increases in the shortwave radiation do not translate to increased SSTs, because more active ocean mesoscale dynamics counteract the development of shallow surface heating layers. Future work to examine these relationships in observational data is warranted.

Detailed comparisons with the CERA system (comparing left and right columns in Fig. 11) indicate that the ocean–eddy-parameterized ensembles still capture strong correlations in

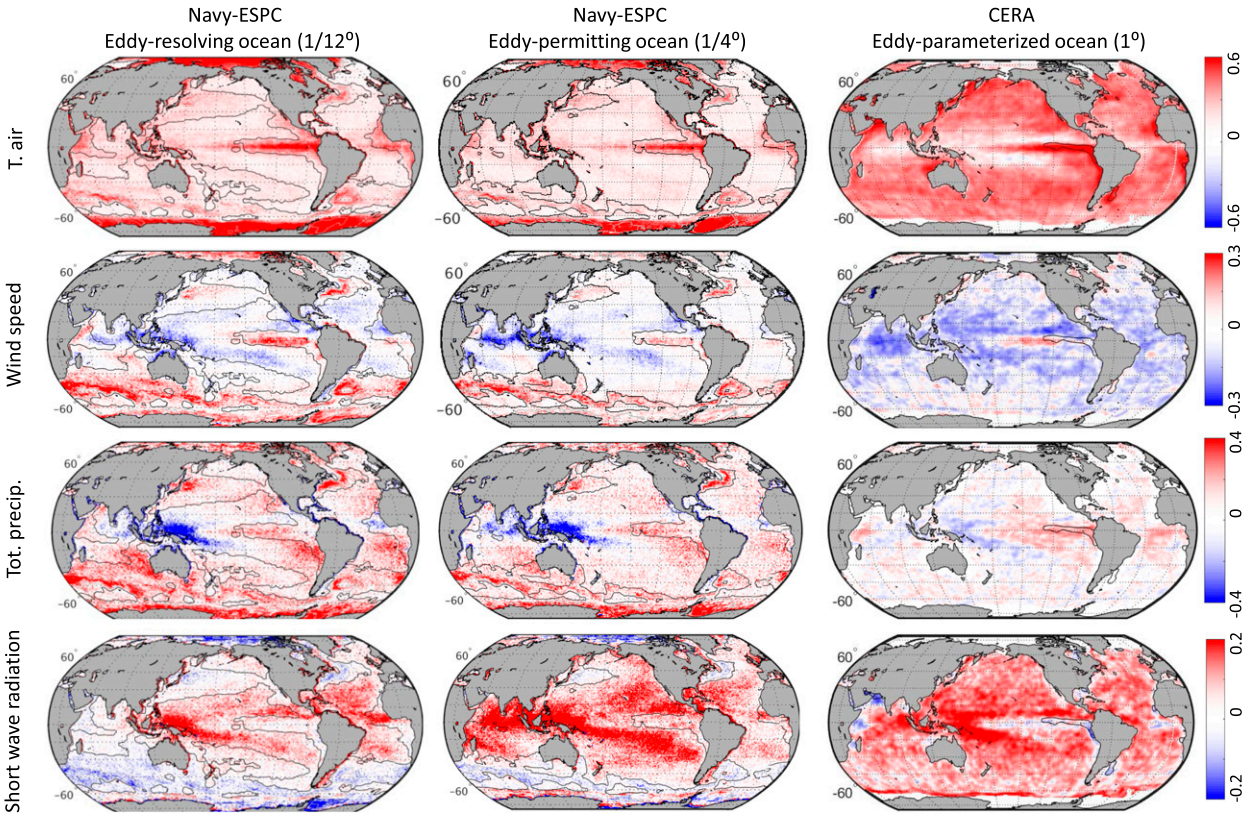

FIG. 11. Comparison of annual average correlation between SST and (from top to bottom) 2 m temperature, 10 m wind speed, total precipitation, and shortwave radiation.

the TEPAC region and the seasonal cycle with enhanced correlations in midlatitude summer [not shown but consistent with findings of Feng et al. (2018) and Laloyaux et al. (2018)]. The 1° model is capable of representing equatorial upwelling and the associated tropical instability waves with a Rossby radius of deformation on the order of 250 km. The CERA system is also capable of resolving the seasonal shallowing of the midlatitude mixed layer as it is driven by the weakening of the atmospheric winds during summer.

However, the CERA system does not exhibit strong correlations associated with the meanders of the Gulf Stream, since the Rossby radius of ~20 km is smaller than the ocean grid resolution of ~100 km. The CERA system also does not capture the interaction between the atmospheric convection and the shallow ocean mixed layer that occurs in the Navy-ESPC system [section 4a(3)]. While the CERA and the Navy-ESPC systems differ in many aspects, this lack of interaction between tropical convection and the ocean mixed layer is due to the relatively coarse (10 m) near-surface vertical model layer thickness in the CERA system. By contrast, the Navy-ESPC uses a hybrid vertical coordinate with the top ocean level thickness of 1 m and an adaptive vertical coordinate that can resolve the vertical density gradients below the mixed layer. Recall that the MLD is often shallower than 20 m in the tropical India Ocean and the Warm pool areas (Figs. 4e,f). Overall, outside of the TEPAC region, the correlations in the CERA system are primarily indicative of the atmosphere driving the ocean, with very little indication of the ocean driving the atmosphere as seen in systems with an eddy-resolving ocean (S. P. Bishop et al. 2017) and in the observation-based literature cited in sections 2 and 4a(1).

6. Summary and conclusions

This paper presents for the first time a systematic review of coupled, short-term OA correlations in an ocean-eddy-resolving ensemble simulation of the Earth system. Similar to previous studies, we find that OA coupling (as measured by the correlations in this study) is prominent in the regions of strong SST gradients, such as western boundary currents (Gulf Stream, Kuroshio, Aghulas, and Falklands Current retroflection regions), equatorial upwelling (tropical east Pacific), and in the eastern boundary upwelling regions. In these regions, the correlations suggest that short-term OA interactions are driven (modulated) by the mesoscale dynamics of the ocean fronts, where ocean dynamics can create strong SST fronts that drive the patterns of turbulent and radiative fluxes with the atmosphere. Consistent with the previous literature, we find that, in regions with strong SST gradients, ocean perturbations drive the atmosphere. Diagnosis of the specific mechanisms for how the SST gradients influence the atmosphere (described in section 2) is beyond the scope of this paper.

In addition to documenting the influence of strong SST gradients, we show that a shallowing of the ocean mixed layer modulates the strength of the OA correlations. It appears that OA coupling is strongest when the MLD is shallower than 20–40 m. Such periods of shallow mixed layer depth are associated with synoptic or seasonal weakening of the atmospheric wind speeds. During these shallow MLD periods, the atmosphere drives the ocean. The ocean mixed layer is generally shallow in midlatitudes during summer and in the tropics (Figs. 4e,f and 7a). Our data also suggest that midlatitude regions can shift from atmosphere-driven ocean during summer to ocean-driven atmosphere in winter.

The reversal of the sign of the OA correlations and its relation to MLD in the midlatitudes does not appear to have been documented in the literature. A comprehensive diagnosis of the process controlling the OA flux correlations will involve a careful examination of the fluxes, the MLD, and possibly a linear perturbation analysis, which are beyond the scope of this study. Short of such detailed examination, we hypothesize that this new finding can be attributed to the way our dataset is constructed. As the coupled Navy ESPC ensembles are cycled, they develop small perturbations in the ocean temperature within the mixed layer (on the order of 0.2–0.4 K according to Fig. 4b), which is comparable to the typical SST uncertainty of 0.5–0.7 K in an ocean DA system (Cummings and Smedstad 2014). Because of the thermal inertia of temperature perturbations in a deep mixed layer, the atmosphere will respond to these SST perturbations. It would be difficult to discern such correlations using a traditional analysis of monthly anomalies, which are likely dominated by synoptic storm variability typical in midlatitude winter. In contrast, all our ensemble members share the same, slightly perturbed, synoptic environments that occur during the analysis time. Hence, the reversed OA correlations can be interpreted as the impact that uncertainty in the SST analysis exerts on the overlaying ensemble of atmospheric circulations.

Finally, we show that in the tropical ocean, the intensity of OA coupling is modulated by the daily variations in atmospheric convective activity. In the ensemble members with less active atmospheric convection, the atmospheric state tends to have fewer clouds, less precipitation, and lighter winds (see summary in Fig. 8). In these ensemble members, the shortwave radiation into the ocean is increased and the wind-driven mixing is suppressed, which leads to increased SST and shallower MLD. In contrast, for the ensemble members with more active atmospheric convection, the SST is decreased due to a combination of more active wind-driven mixing and lower incoming shortwave radiation (see Fig. 8 for a graphical summary).

Our model of atmospheric-driven modulation of OA fluxes in the tropical ocean is in contrast to the conventional understanding that significant SST perturbations can modulate convective activity. We attribute this again to the design of our experiment, which is focused on 24-h coupled forecasts initialized with small variations of the SST around an analyzed ocean state. In our case, minor variations of the SST do not appear to affect the convective activity (as evidenced by the precipitation rates) and instead the convective activity is modulated by small perturbations to the atmospheric state that can trigger highly nonlinear threshold criteria in the atmospheric convective parameterization. Further study is needed to see if this mechanism is replicated in a convection-resolving model or supported by observational data that account for the seasonal cycle.

Comparisons of the OA correlations that were retrieved from the eddy-resolving Navy-ESPC model with the OA correlations retrieved from the ECMWF parameterized eddy model and the eddy-permitting version of the Navy-ESPC model further demonstrate the need for eddy-resolving ocean modeling to properly characterize patterns of OA coupling. For example, the CERA model with a 1° ocean model and 10 m first ocean layer thickness only captures OA correlations in the summer midlatitudes and in the tropical east Pacific (where the ocean model resolves the ocean Rossby radius of deformation). These findings are consistent with Feng et al. (2018) and Laloyaux et al. (2018) that show coupling in the CERA dataset only in the midlatitudes and the TEPAC region and do not show any coupling in the western boundary regions or in the tropical Indian and west Pacific Oceans. The comparison with the eddy-permitting version of the Navy-ESPC model indicates that a lower resolution ocean responds more directly to the perturbations in the atmospheric conditions and hence SSTs can warm more readily in response to positive perturbations in surface fluxes. In addition, simulation with the eddy-permitting ocean has significantly lower SST variability around ocean fronts, which decreases the ability of the ocean to drive atmospheric properties. As a result, the direction of the OA fluxes in coupled models that do not resolve ocean mesoscale variability properly is predominantly from the atmosphere into the ocean. These results motivate the development of new methods to verify the strength of OA coupling in coupled models against observations. One such promising method is based on cross-spectral correlations computed from the scatterometer wind and SST observations presented in Laurindo et al. (2019).

Patterns of short-term OA correlations found here support the importance of coupled modeling for short-term Earth system forecasts. Our findings also suggest that the implementation of strongly coupled data assimilation would require specification of flow-dependent correlations either through localized ensembles (e.g., as used in Sluka et al. 2016; Frolov et al. 2016) or through coupled tangent linear models (C. H. Bishop et al. 2017). This further supports findings by Smith et al. (2017) that coupled correlations have significant flow and state dependence. However, our findings also suggest that average correlations across the ocean–atmosphere interface can be quite low, especially away from the strong boundary currents and regions with active atmospheric convection. This is in contrast to correlations within a single fluid that decay exponentially with distance from the observation. Despite the modest magnitude of the averaged cross-fluid OA correlations found in this study, it is likely that locally in time and space the OA correlations can be much larger. This would be consistent with the recent findings that a small number of extreme events might be dominating the average OA exchange (Parfitt and Czaja 2016; O'Neill et al. 2017). Furthermore, the small, short-term OA correlations might increase if averaged over time

(Feng et al. 2018), this might impact the skill of the subseasonal and seasonal forecasts that often look at weekly and monthly averaged forecasts respectfully. However, to distinguish cases where these correlations are significant will likely require a larger number of ensemble members than is a common practice at present.

Further progress in coupled data assimilation and forecasting will require extra attention to the specification of these modest OA correlations. Our comparisons of the OA correlations in the systems with coarser ocean resolution also suggest that the OA correlations in non-eddy-resolving models might be significantly different from the actual OA balances present in nature, which would require additional care when observations are assimilated into a coupled model. For example, an ensemble of eddy-parameterized models will suggest that a warm SST innovation (a mismatch between the observation and the forecast) in the Gulf Stream region should translate to reduced cloud cover and weaker winds in the atmosphere, which is the opposite of how the actual atmosphere may respond. Mitigation of such misrepresentation of coupled correlations with small and imperfect ensembles will motivate further development of advanced localization strategies and novel uses of representation error in coupled DA.

Acknowledgments. This work was supported by N2N6E and the U.S. Office of Naval Research through the Navy Earth Systems Prediction Capability Project (PE 0603207N). This research was partially supported by the Physical Sciences Laboratory of the NOAA Earth System Research Laboratories. We are grateful for access to the Department of Defense high performance computing resources that enabled us to conduct this research. We are thankful to Hyodae Seo, Aneesh Subramanian, and Kathy Pegion for helpful and encouraging comments on the early versions of the manuscript. We thank Laura Slivinski for providing an internal review of this manuscript.

Data availability statement. CERA 20C was downloaded from the publicly available ECMWF MARS server. Navy-ESPC simulation data have not been released for public access.

APPENDIX

Computation of Statistical Quantities

a. Computation of OA correlations

OA correlations described in this paper are computed using the following steps:

1) First, we remove the diurnal variability from the fields by computing a daily average of ocean and atmospheric fields:

$$x^{24}(t) = \frac{1}{N_\tau}\sum_{\tau=0}^{24} x_\tau(t), \tag{A1}$$

where $x^{24}(t)$ is the 24-h average of a variable x (such as sea surface temperature), τ is the forecast length in hours, t is the specific start time for the forecast, and x^τ is the instantaneous forecast for the forecast lead τ. Using a series of sensitivity experiments, we established that averaging over the $\tau = 12$ and $\tau = 24$ forecasts provided ensemble correlations least affected by the model spinup within the first day of the forecast window. Specifically, the average of $\tau = 12$ and $\tau = 24$ correlations was very similar to the correlations from a free-running model computed using 6-hourly increments over day 3 of the forecast (from $\tau = 48$ to $\tau = 72$ using 6-hourly increments). This finding is consistent with the finding of Laloyaux et al. (2018) who found that in the CERA system, the ocean and the atmosphere come in to the adjustment within the first 12 h of the forecast.

2) Then, correlation $c_{\text{var1|var2}}$ for a single short-lead forecast was computed:

$$c^t_{\text{var1|var2}} = \text{corr}(\text{var1};\text{var2})^t = \frac{\sum_{i=1}^{N_{\text{ens}}}\left[\left(\{x^{24}_{\text{var1}}\}^t_i - \overline{\{x^{24}_{\text{var1}}\}^t}\right)\left(\{x^{24}_{\text{var2}}\}^t_i - \overline{\{x^{24}_{\text{var2}}\}^t}\right)\right]}{\sqrt{\sum_{i=1}^{N_{\text{ens}}}\left[\left(\{x^{24}_{\text{var1}}\}^t_i - \overline{\{x^{24}_{\text{var1}}\}^t}\right)\right]^2}\sqrt{\sum_{i=1}^{N_{\text{ens}}}\left[\left(\{x^{24}_{\text{var2}}\}^t_i - \overline{\{x^{24}_{\text{var2}}\}^t}\right)\right]^2}}, \tag{A2}$$

where var1 and var2 are variable labels such as air temperature or ocean temperature, t is the start date of the ensemble forecast, for example 1 August 2017, i is the ensemble member index (from 1 to N_{ens}), and overbar denotes the ensemble average for this start date.

We chose to focus in Eq. (A2) on the zero-lag correlations between daily averages as they are most relevant to the problem of coupled DA. Specifically, most existing coupled DA system (Lea et al. 2015; Laloyaux et al. 2015; Holt et al. 2011; Barton et al. 2021) use DA windows between 6 and 24 h in length. Any lagged correlations between daily averages are not addressed explicitly by the DA system and are instead generated by the coupled forecast model (e.g., Komori et al. 2018). These implicit lagged correlations are relevant to drivers of multiweek predictability and their study lies outside of the scope of this paper.

3) Finally, when needed, an annual average of short-term correlations in Eq. (A2) was computed as following:

$$c^{\text{annual}}_{\text{var1|var2}} = \frac{1}{N_t}\sum_{t=0}^{52} c^t_{\text{var1|var2}}, \tag{A3}$$

where the summation in Eq. (A3) is over the $N_t = 52$ weekly forecasts.

It should be noted that averaging of the correlations in Eq. (A3) increases the effective ensemble size and reduces sampling noise in the correlation computation. For example,

given the same p value of 0.05, the instantaneous correlation in Eq. (A2) is statically significantly different from zero when it is larger than 0.47, while the annual average in Eq. (A3) is significant at much lower cutoff of 0.07. The downside of the averaging over the annual cycle is that it highlights the regions that have stationary statistics (when the sign and the magnitude of the correlation is similar through the year). In regions where correlations have a significant annual cycle, the annual average may not be meaningful. Hence, in addition to the annual averages of correlations, we also examine the seasonal cycles of correlations for each of the study regions highlighted here.

b. *Computation of the annual average of the standard deviation*

To compute the annual average of the ensemble standard deviation, we used the following formula that first averaged variances for each individual start time before taking the square root of the average variance:

$$\mathrm{std}_{\mathrm{var}}^{\mathrm{annual}} = \sqrt{\frac{1}{52}\sum_{t=0}^{52}\{\mathrm{var}[X_{\mathrm{var}}(t)]\}}, \tag{A4}$$

where $X_{\mathrm{var}}(t)$ is the ensemble of fields for the target variable "var" valid for time t.

REFERENCES

Alexander, M. A., and C. Penland, 1996: Variability in a mixed layer ocean model driven by stochastic atmospheric forcing. *J. Climate*, **9**, 2424–2442, https://doi.org/10.1175/1520-0442(1996)009<2424:VIAMLO>2.0.CO;2.

——, J. D. Scott, and C. Deser, 2000: Processes that influence sea surface temperature and ocean mixed layer depth variability in a coupled model. *J. Geophys. Res.*, **105**, 16 823–16 842, https://doi.org/10.1029/2000JC900074.

Barton, N., and Coauthors, 2021: The Navy's Earth System Prediction Capability: A new global coupled atmosphere-ocean-sea ice prediction system designed for daily to subseasonal forecasting. *Earth Space Sci.*, https://doi.org/10.1029/2020EA001199, in press.

Bishop, C. H., S. Frolov, D. R. Allen, D. D. Kuhl, and K. Hoppel, 2017: The local ensemble tangent linear model: An enabler for coupled model 4DVAR. *Quart. J. Roy. Meteor. Soc.*, **143**, 1009–1020, https://doi.org/10.1002/qj.2986.

Bishop, S. P., R. J. Small, F. O. Bryan, and R. A. Tomas, 2017: Scale dependence of midlatitude air–sea interaction. *J. Climate*, **30**, 8207–8221, https://doi.org/10.1175/JCLI-D-17-0159.1.

Bleck, R., 2002: An oceanic general circulation model framed in hybrid isopycnic-Cartesian coordinates. *Ocean Modell.*, **4**, 55–88, https://doi.org/10.1016/S1463-5003(01)00012-9.

Bowler, N. E., and Coauthors, 2017: Inflation and localisation tests in the development of an ensemble of 4D-ensemble variational assimilations. *Quart. J. Roy. Meteor. Soc.*, **143**, 1280–1302, https://doi.org/10.1002/qj.3004.

Byrne, D., M. Münnich, I. Frenger, and N. Gruber, 2016: Mesoscale atmosphere ocean coupling enhances the transfer of wind energy into the ocean. *Nat. Commun.*, **7**, ncomms11867, https://doi.org/10.1038/ncomms11867.

Cayan, D. R., 1992: Latent and sensible heat flux anomalies over the northern oceans: Driving the sea surface temperature. *J. Phys. Oceanogr.*, **22**, 859–881, https://doi.org/10.1175/1520-0485(1992)022<0859:LASHFA>2.0.CO;2.

Chelton, D. B., and S.-P. Xie, 2010: Coupled ocean-atmosphere interaction at oceanic mesoscales. *Oceanography*, **23**, 52–69, https://doi.org/10.5670/oceanog.2010.05.

——, and Coauthors, 2001: Observations of coupling between surface wind stress and sea surface temperature in the eastern tropical Pacific. *J. Climate*, **14**, 1479–1498, https://doi.org/10.1175/1520-0442(2001)014<1479:OOCBSW>2.0.CO;2.

——, M. G. Schlax, M. H. Freilich, and R. F. Milliff, 2004: Satellite measurements reveal persistent small-scale features in ocean winds. *Science*, **303**, 978–983, https://doi.org/10.1126/science.1091901.

Cummings, J. A., and O. M. Smedstad, 2014: Ocean data impacts in global HYCOM. *J. Atmos. Oceanic Technol.*, **31**, 1771–1791, https://doi.org/10.1175/JTECH-D-14-00011.1.

Deser, C., J. Bates, and S. Wahl, 1993: The influence of sea surface temperature gradients on stratiform cloudiness along the equatorial front in the Pacific Ocean. *J. Climate*, **6**, 1172–1180, https://doi.org/10.1175/1520-0442(1993)006<1172:TIOSST>2.0.CO;2.

Fairall, C. W., E. F. Bradley, J. E. Hare, A. A. Grachev, and J. B. Edson, 2003: Bulk parameterization of air-sea fluxes: Updates and verification for the COARE algorithm. *J. Climate*, **16**, 571–591, https://doi.org/10.1175/1520-0442(2003)016<0571:BPOASF>2.0.CO;2.

Feng, X., K. Haines, and E. de Boisséson, 2018: Coupling of surface air and sea surface temperatures in the CERA-20C reanalysis. *Quart. J. Roy. Meteor. Soc.*, **144**, 195–207, https://doi.org/10.1002/qj.3194.

Frenger, I., N. Gruber, R. Knutti, and M. Münnich, 2013: Imprint of Southern Ocean eddies on winds, clouds and rainfall. *Nat. Geosci.*, **6**, 608–612, https://doi.org/10.1038/ngeo1863.

Frolov, S., C. H. Bishop, T. R. Holt, J. A. Cummings, and D. D. Kuhl, 2016: Facilitating strongly coupled ocean–atmosphere data assimilation with an interface solver. *Mon. Wea. Rev.*, **144**, 3–20, https://doi.org/10.1175/MWR-D-15-0041.1.

——, W. Campbel, B. Ruston, C. H. Bishop, D. D. Kuhl, M. K. Flatau, and J. G. McLay, 2020: Assimilation of low-peaking satellite observations using the coupled interface framework. *Mon. Wea. Rev.*, **148**, 637–654, https://doi.org/10.1175/MWR-D-19-0029.1.

Hayes, S. P., M. J. McPhaden, and J. M. Wallace, 1989: The influence of sea-surface temperature on surface wind in the eastern equatorial Pacific: Weekly to monthly variability. *J. Climate*, **2**, 1500–1506, https://doi.org/10.1175/1520-0442(1989)002<1500:TIOSST>2.0.CO;2, .

Hewitt, H. T., and Coauthors, 2016: The impact of resolving the Rossby radius at mid-latitudes in the ocean: Results from a high-resolution version of the Met Office GC2 coupled model. *Geosci. Model Dev.*, **9**, 3655–3670, https://doi.org/10.5194/gmd-9-3655-2016.

Hill, C., C. DeLuca, B. Balaji, M. Suarez, and A. Da Silva, 2004: The architecture of the earth system modeling framework. *Comput. Sci. Eng.*, **6**, 18–28, https://doi.org/10.1109/MCISE.2004.1255817.

Hobbs, P. V., 1987: The Gulf Stream rainband. *Geophys. Res. Lett.*, **14**, 1142–1145, https://doi.org/10.1029/GL014i011p01142.

Hogan, T. F., 2007: Land surface modeling in the Navy Operational Global Atmospheric Prediction System. *22nd Conf. on Weather Analysis and Forecasting/18th Conf. on Numerical Weather Prediction*, Park City, UT, Amer. Meteor. Soc., 11B.1, https://ams.confex.com/ams/22WAF18NWP/techprogram/paper_123403.htm.

——, and Coauthors, 2014: The Navy Global Environmental Model. *Oceanography*, **27**, 116–125, https://doi.org/10.5670/oceanog.2014.73.

Holt, T. R., J. A. Cummings, C. H. Bishop, J. D. Doyle, X. Hong, S. Chen, and Y. Jin, 2011: Development and testing of a coupled ocean–atmosphere mesoscale ensemble prediction system. *Ocean Dyn.*, **61**, 1937–1954, https://doi.org/10.1007/s10236-011-0449-9.

Houtekamer, P. L., L. Lefaivre, J. Derome, H. Ritchie, and H. L. Mitchell, 1996: A system simulation approach to ensemble prediction. *Mon. Wea. Rev.*, **124**, 1225–1242, https://doi.org/10.1175/1520-0493(1996)124<1225:ASSATE>2.0.CO;2.

Hunke, E. C., and W. H. Lipscomb, 2015: CICE: The Los Alamos Sea Ice Model documentation and software user's manual version 4.0. Los Alamos National Laboratory, 72 pp.

Isaksen, L., M. Bonavita, R. Buizza, M. Fisher, J. Haseler, M. Leutbecher, and L. Raynaud, 2010: Ensemble of data assimilations at ECMWF. ECMWF Tech. Memo. 636, 48 pp., https://doi.org/10.21957/obke4k60.

Kain, J. S., and J. M. Fritsch, 1990: A one-dimensional entraining/detraining plume model and its application in convective parameterization. *J. Atmos. Sci.*, **47**, 2784–2802, https://doi.org/10.1175/1520-0469(1990)047<2784:AODEPM>2.0.CO;2.

Kara, A. B., H. E. Hurlburt, and A. J. Wallcraft, 2005: Stability-dependent exchange coefficients for air–sea fluxes. *J. Atmos. Oceanic Technol.*, **22**, 1080–1094, https://doi.org/10.1175/JTECH1747.1.

Kilpatrick, T., N. Schneider, and B. Qiu, 2016: Atmospheric response to a midlatitude SST front: Alongfront winds. *J. Atmos. Sci.*, **73**, 3489–3509, https://doi.org/10.1175/JAS-D-15-0312.1.

Kirtman, B. P., and Coauthors, 2012: Impact of ocean model resolution on CCSM climate simulations. *Climate Dyn.*, **39**, 1303–1328, https://doi.org/10.1007/s00382-012-1500-3.

Komori, N., T. Enomoto, T. Miyoshi, A. Yamazaki, A. Kuwano-Yoshida, and B. Taguchi,2018: Ensemble-based atmospheric reanalysis using a global coupled atmosphere–ocean GCM. *Mon. Wea. Rev.*, **146**, 3311–3323, https://doi.org/10.1175/MWR-D-17-0361.1.

Kuhl, D. D., T. E. Rosmond, C. H. Bishop, J. McLay, and N. L. Baker, 2013: Comparison of hybrid ensemble/4DVar and 4DVar within the NAVDAS-AR data assimilation framework. *Mon. Wea. Rev.*, **141**, 2740–2758, https://doi.org/10.1175/MWR-D-12-00182.1.

Laloyaux, P., M. Balmaseda, D. Dee, K. Mogensen, and P. Janssen, 2015: A coupled data assimilation system for climate reanalysis. *Quart. J. Roy. Meteor. Soc.*, **142**, 65–78, https://doi.org/doi:10.1002/qj.2629.

——, S. Frolov, B. Menetrier, and M. Bonavita, 2018: Implicit and explicit cross-correlations in coupled data assimilation. *Quart. J. Roy. Meteor. Soc.*, **144**, 1851–1863, https://doi.org/10.1002/qj.3373.

Laurindo, L. C., L. Siqueira, A. J. Mariano, and B. P. Kirtman, 2019: Cross-spectral analysis of the SST/10-m wind speed coupling resolved by satellite products and climate model simulations. *Climate Dyn.*, **52**, 5071–5098, https://doi.org/10.1007/s00382-018-4434-6.

Lea, D. J., I. Mirouze, M. J. Martin, R. R. King, A. Hines, D. Walters, and M. Thurlow, 2015: Assessing a new coupled data assimilation system based on the Met Office coupled atmosphere–land–ocean–sea ice model. *Mon. Wea. Rev.*, **143**, 4678–4694, https://doi.org/10.1175/MWR-D-15-0174.1.

Lindzen, R. S., and S. Nigam, 1987: On the role of sea surface temperature gradients in forcing low-level winds and convergence in the tropics. *J. Atmos. Sci.*, **44**, 2418–2436, https://doi.org/10.1175/1520-0469(1987)044<2418:OTROSS>2.0.CO;2.

Ma, X., and Coauthors, 2016: Western boundary currents regulated by interaction between ocean eddies and the atmosphere. *Nature*, **535**, 533–537, https://doi.org/10.1038/nature18640.

Masumoto, Y., and Coauthors, 2004: A fifty-year eddy-resolving simulation of the world ocean: Preliminary outcomes of OFES (OGCM for the Earth Simulator). *J. Earth Simul.*, **1**, 35–56.

Matthews, A. J., D. B. Baranowski, K. J. Heywood, P. J. Flatau, and S. Schmidtko, 2014: The surface diurnal warm layer in the Indian Ocean during CINDY/DYNAMO. *J. Climate*, **27**, 9101–9122, https://doi.org/10.1175/JCLI-D-14-00222.1.

Meehl, G. A., 1987: The annual cycle and interannual variability in the tropical Pacific and Indian Ocean regions. *Mon. Wea. Rev.*, **115**, 27–50, https://doi.org/10.1175/1520-0493(1987)115<0027:TACAIV>2.0.CO;2.

Metzger, J., and Coauthors, 2014: U.S. Navy operational global ocean and Arctic ice prediction systems. *Oceanography*, **27**, 32–43, https://doi.org/10.5670/oceanog.2014.66.

Minobe, S., A. Kuwano-Yoshida, N. Komori, S. P. Xie, and R. J. Small, 2008: Influence of the Gulf Stream on the troposphere. *Nature*, **452**, 206–209, https://doi.org/10.1038/nature06690.

O'Neill, L. W., T. Haack, D. B. Chelton, and E. Skyllingstad, 2017: The Gulf Stream convergence zone in the time-mean winds. *J. Atmos. Sci.*, **74**, 2383–2412, https://doi.org/10.1175/JAS-D-16-0213.1.

Parfitt, R., and A. Czaja, 2016: On the contribution of synoptic transients to the mean atmospheric state in the Gulf Stream region. *Quart. J. Roy. Meteor. Soc.*, **142**, 1554–1561, https://doi.org/10.1002/qj.2689.

Penny, S. G., and Coauthors, 2017: Coupled data assimilation for integrated earth system analysis and prediction: Goals, challenges and recommendations. WWRP 2017-3, 59 pp., https://www.wmo.int/pages/prog/arep/wwrp/new/documents/Final_WWRP_2017_3_27_July.pdf.

Pullen, J., and Coauthors, 2017: Coupled ocean-atmosphere forecasting at short and medium time scales. *J. Mar. Res.*, **75**, 877–921, https://doi.org/10.1357/002224017823523991.

Putrasahan, D. A., A. J. Miller, and H. Seo, 2013: Isolating mesoscale coupled ocean-atmosphere interactions in the Kuroshio Extension region. *Dyn. Atmos. Oceans*, **63**, 60–78, https://doi.org/10.1016/j.dynatmoce.2013.04.001.

Ridout, J. A., Y. Jin, and C. S. Liou, 2005: A cloud-base quasi-balance constraint for parameterized convection: Application to the Kain–Fritsch cumulus scheme. *Mon. Wea. Rev.*, **133**, 3315–3334, https://doi.org/10.1175/MWR3034.1.

Saha, S., and Coauthors, 2010: The NCEP Climate Forecast System Reanalysis. *Bull. Amer. Meteor. Soc.*, **91**, 1015–1058, https://doi.org/10.1175/2010BAMS3001.1.

Saravanan, R., and P. Chang, 2019: Midlatitude mesoscale ocean-atmosphere interaction and its relevance to S2S prediction. *Sub-Seasonal to Seasonal Prediction: The Gap between Weather and Climate Forecasting*, A. W. Robertson and F. Vitart, Eds., Elsevier, 183–200.

Schneider, N., and B. Qiu, 2015: The atmospheric response to weak sea surface temperature fronts. *J. Atmos. Sci.*, **72**, 3356–3377, https://doi.org/10.1175/JAS-D-14-0212.1.

Sluka, T. C., S. G. Penny, E. Kalnay, and T. Miyoshi, 2016: Assimilating atmospheric observations into the ocean using strongly coupled ensemble data assimilation. *Geophys. Res. Lett.*, **43**, 752–759, https://doi.org/10.1002/2015GL067238.

Small, R. J., and Coauthors, 2008: Air-sea interaction over ocean fronts and eddies. *Dyn. Atmos. Oceans*, **45**, 274–319, https://doi.org/10.1016/j.dynatmoce.2008.01.001.

——, F. O. Bryan, S. P. Bishop, and R. A. Tomas, 2019: Air–sea turbulent heat fluxes in climate models and observational

analyses: What drives their variability? *J. Climate*, **32**, 2397–2421, https://doi.org/10.1175/JCLI-D-18-0576.1.

Smith, P. J., A. S. Lawless, and N. K. Nichols, 2017: Estimating forecast error covariances for strongly coupled atmosphere–ocean 4D-var data assimilation. *Mon. Wea. Rev.*, **145**, 4011–4035, https://doi.org/10.1175/MWR-D-16-0284.1.

Theurich, G., and Coauthors, 2016: The earth system prediction suite: Toward a coordinated U.S. modeling capability. *Bull. Amer. Meteor. Soc.*, **97**, 1229–1247, https://doi.org/10.1175/BAMS-D-14-00164.1.

Vitart, F., and M. Balmaseda, 2018: Impact of sea surface temperature biases on extended-range forecasts. ECMWF Tech. Memo. 830, 21 pp., https://doi.org/10.21957/xvbl914ps.

Wallace, J. M., T. P. Mitchell, and C. Deser, 1989: The influence of sea-surface temperature on surface wind in the eastern equatorial Pacific: Seasonal and interannual variability. *J. Climate*, **2**, 1492–1499, https://doi.org/10.1175/1520-0442(1989)002<1492:TIOSST>2.0.CO;2.

Wu, R., and B. P. Kirtman, 2007: Regimes of seasonal air-sea interaction and implications for performance of forced simulations. *Climate Dyn.*, **29**, 393–410, https://doi.org/10.1007/s00382-007-0246-9.

Xie, S. P., 2004: Satellite observations of cool ocean–atmosphere interaction. *Bull. Amer. Meteor. Soc.*, **85**, 195–208, https://doi.org/10.1175/BAMS-85-2-195.